Synthesis and Electrical Characterization of Oligo(phenylene ethynylene) Molecular Wires Coordinated to Transition Metal Complexes

Zhaoyue Ng,[†] Kian Ping Loh,[†,*] Liqian Li,[†] Peter Ho,[‡] Ping Bai,[§] and John H. K. Yip[†,*]

[†]Department of Chemistry, National University of Singapore, 3 Science Drive 3, Singapore 117543, [‡]Department of Physics, National University of Singapore, Lower Kent Ridge Road, Singapore 117542, and [§]Institute of High Performance Computing, 1 Fusionpolis Way, Singapore 138132

ABSTRACT Organometallic wires are interesting alternatives to conventional molecular wires based on a pure organic system because of the presence of d orbitals in the transition metal complex. However, synthetic problems, such as decreased stability of the compounds when labile metal complexes are present, often impede their isolation in a pure state and preclude a rapid development of such hybrid molecular wires. In this work, we show that preassembled self-assembled monolayers (SAM) based on pyridine-terminated 1-((4-acetylthiophenyl)ethynyl)-4-((4-pyridyl)ethynyl)benzene can act as a template for the architectural build up of a second layer of transition metal complexes to form an array of organometallic molecular wires on gold. Ru^{II}(terpy)(bipy)$^{2+}$ (terpy = 2,2′:6′,2′′-terpyridine and bipy = 2,2′-bipyridine) or cyclometalated Pt^{II}(pbipy) (pbipy = 6-phenyl-2,2′-bipyridine) were axially coordinated onto the organic SAM *via* its terminal pyridinium moieties. Current−voltage studies show that the electronic coupling between the transition metal and organic wire produces a molecular wire that exhibits higher conductance than the original organic chain. The presence of the transition metal complexes in the hybrid molecular wire introduces distinctive negative differential resistance (NDR) effects.

KEYWORDS: molecular wire · negative differential resistance · molecular electronics · scanning tunneling microscopy · self-assembly

In order for molecular electronics to be viable for future semiconductor nanoelectronics, there are various complex challenges to be addressed. Wide ranging issues include the architecture of the molecule, metal−molecule interconnects, electronic communication schemes both at the intra- and at the intermolecule level, as well as the chemistry concerning the self-assembly and stabilization of the molecular wires.[1,2] Central to the design of molecular self-assembly is that self-assembly should occur readily at interconnect junctions. What has not been considered so far is whether these preassembled SAMs can act as a template for the architectural build up of a second layer containing metal ions, as such design can hold promise for modulating the transport and switching properties at nanojunctions. Despite their unique electronic properties, there are relatively few studies of molecular wires containing transition metal.[3] Most of the molecular wires studied to date are constructed entirely of delocalized orbital networks in organic chains. Unfortunately, all-organic molecules show conductivities which are orders of magnitudes lower than that predicted by theory.[4,5] The π-systems are relatively monotonous in terms of design and suffer from limitations to the type of elements and molecular motifs that can be incorporated. Molecular wires incorporating transition metal complexes are interesting due to the availability of multiple redox and spin states that can give rise to large third-order nonlinear susceptibilities.[6] It is possible that the conductance through a conjugated backbone containing a transition metal complex is higher than that of the all-organic system because of the existence of strong electronic coupling between the metal centers and the conjugated organic ligands.[7,8] The d states of the metal atom are higher in energy than the π-bonding orbitals in the conjugated system, thus the molecular level in such hybrid d−π systems will lie close to the Fermi level of the metal electrodes. One attraction of such hybrid molecular wires is that the electronic properties of the wire can be tuned by either varying the ancillary ligands present on the metal centers or changing the oxidation states of the metal.[9]

In this study, we devised a two-step strategy to construct self-assembled films by using a new pyridine-terminated molecular wire (1-((4-acetylthiophenyl)ethynyl)-4-((4-pyridyl)ethynyl)benzene) (abbreviated as OPP, Scheme 1) as a platform for coordination with transition metal complexes.

*Address correspondence to chmlohkp@nus.edu.sg, chmyiphk@nus.edu.sg.

Received for review February 17, 2009 and accepted July 20, 2009.

Published online July 29, 2009.
10.1021/nn900570v CCC: $40.75

© 2009 American Chemical Society

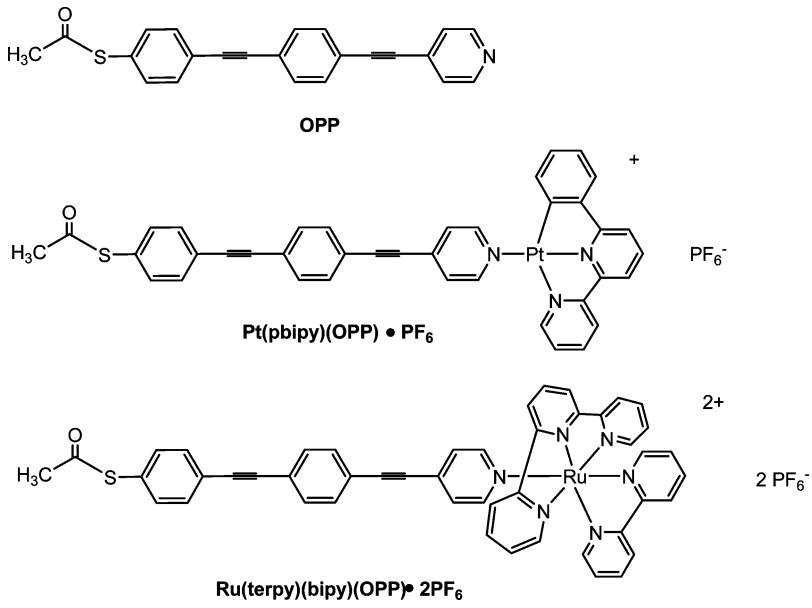

Scheme 1. Chemical structures of the OPP, Pt-OPP, and Ru-OPP molecular wires.

OPP was first self-assembled on gold substrate to form a well-ordered and compact monolayer. Subsequently, $Ru^{II}(terpy)(bipy)^{2+}$ (terpy = 2,2′:6′,2′′-terpyridine and bipy = 2,2′-bipyridine) or cyclometalated $Pt^{II}(pbipy)$ (pbipy = 6-phenyl-2,2′-bipyridine) was axially coordinated onto the OPP SAM *via* the terminal pyridyl moieties (abbreviated as Ru-OPP or Pt-OPP, respectively). The Pt^{II} complex was chosen because of the rich photophysics of cyclometalated Pt^{II} complexes.[10,11] More importantly, the Pt^{II} complex has potential in chemical sensing[12] because its open, coordinatively unsaturated d^8 metal center can interact with substrates. Unlike the Pt complex, the d^6 Ru^{II} complex can undergo reversible oxidation−reduction.[13] Coupling the Ru^{II} center with an OPP should lead to a molecular wire that is redox switchable.

Using this two-step process, an organic−inorganic molecular wire adjoined by a dative bond between the N end of the conjugated organic system and the transition metal center could be constructed; these molecular wires were observed to adopt an upright configuration. In contrast, direct assembly of the synthesized organometallic molecular wire on gold was found to result in strongly tilted molecules that formed defective films. The electrical properties of the composite systems were probed using three test beds, namely, large area sandwich device structures, conducting-probe atomic force microscopy, and scanning tunneling spectroscopy (STS). STM and AFM *I*−*V* measurements revealed interesting nonlinear *I*−*V* phenomena in the organometallic ensemble, including enhanced conductivities and negative differential resistance (NDR). Theoretical calculations of their electronic structures were performed to gain insights into the charge transport properties.

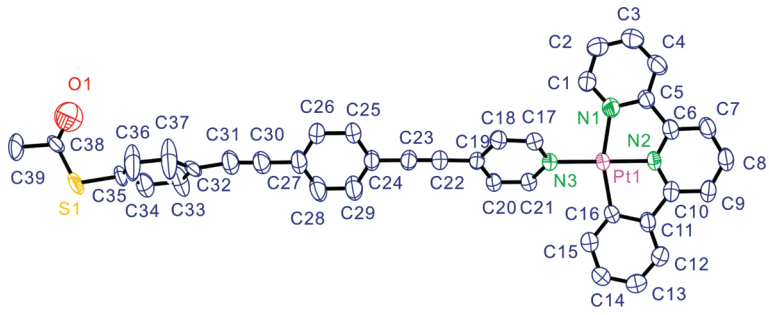

Figure 1. ORTEP plot of Pt(pbipy)(OPP) · PF_6 (thermal ellipsoid: 50%). Pt(1)−N(1) = 2.091(4) Å, Pt(1)−N(2) = 1.961(4) Å, Pt(1)−N(3) = 2.038 (4) Å, Pt(1)−C(16) = 2.037(5) Å, N(1)−Pt(1)−N(2) = 80.07(17)°, N(2)−Pt(1)−N(3) = 177.58(15)°, C(16)−Pt(1)−N(3) = 99.26(17)°, C(16)−Pt(1)−N(1) = 161.18(18)°.

RESULTS AND DISCUSSION

Synthesis and Structure of Organometallic Wires. The OPP was synthesized by Sonogashira coupling of 1-[4-(*S*-acetylthiomethyl)phenyl]acetylene and 4-iodophenylethynylpyridine. Substitution of the labile CH_3CN in the complexes Pt(pbip)-$(NCCH_3)$ · PF_6 and Ru(terpy)(bipy)$(NCCH_3)$ · $2PF_6$ produced the organometallic wires Pt(pbip)(OPP) · PF_6 (abbreviated as Pt-OPP) and Ru(terpy)(bipy)(OPP) · $2PF_6$ (abbreviated as Ru-OPP), respectively. Figure 1 shows the X-ray crystal structure of Pt(pbip)(OPP) · PF_6. The molecule is composed of a rod-like OPP, which is capped by a cyclometalated Pt(pbipy) moiety. The Pt ion is bonded to the pyridyl ring of the OPP and displays a distorted square-planar coordination geometry. The Pt−N and Pt−C bond distances and N−Pt−N and N−Pt−C angles are similar to those of Pt(pbipy)(pyridine)$^+$.

At the other end of the wire is a thioacetyl group. The three six-membered rings are not co-planar; the pyridyl ring shows dihedral angles of 49.5 and 21.0° with the terpyridine (terpy) ligand and the central phenyl ring, respectively. The dihedral angle between the central phenyl ring and the acetylthiophenol ring is 41.9°. The distance between the apical carbon atom of the terpy ligand and the S atom is 2.48 nm, while the Pt−S distance is 2.01 nm.

Organic−inorganic hybrid films were fabricated *via* two routes, namely, the direct assembly or the two-step method, as shown in Figure 2. In the direct assembly method, a molecular wire consisting of the $Pt(pbipy)^+$ complex coupled to thiolated OPP was first synthesized, and the thiolated end of the OPP serves as the bridging ligand to the Au surface. However, the addition of NH_4OH to deprotect the acetyl groups was found to result in the dissociation of the transition metal from the organic wire. Therefore, Pt(pbipy)(OPP) thioacetate derivatives were directly assembled on gold without any base deprotection. Another approach was to first assemble the OPP mono-

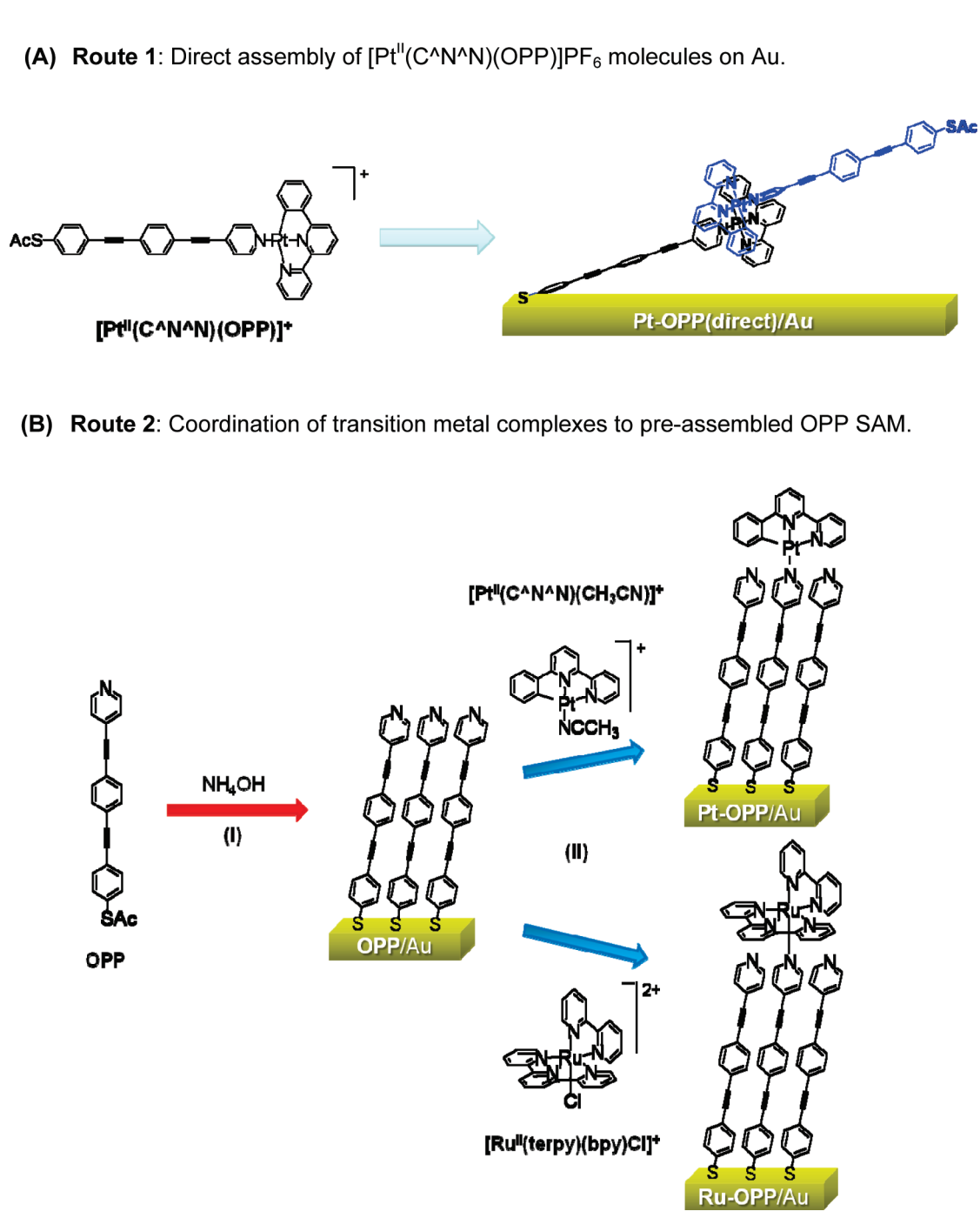

Figure 2. (a) Direct assembly of $[Pt^{II}(C^{\wedge}N^{\wedge}N)(OPP)]PF_6$ molecules on Au resulting in the proposed multilayer structure. (b) Self-assembly of OPP monolayer by *in situ* deprotection of thioacetate precursors and subsequent coordination of Pt(II) and Ru(II) complexes to form organic−inorganic hybrid molecular ensembles.

layer on gold, followed by the axial coordination[14] of the terminal pyridinium moieties of the OPP molecular wire to transition metal complexes. For convenience, in this paper, we call the hybrid molecular wire Pt-OPP. In this case, Au substrates prefunctionalized with OPP SAM were incubated in ~1 mM solution of $Pt(pbipy)(CH_3CN)\cdot PF_6$ in anhydrous acetonitrile for 2 days. A similar procedure was applied for $[Ru^{II}(terpy)(bipy)]$ complexes by heating OPP-modified gold substrates in 1 mM of the precursor solution under nitrogen atmosphere, and the hybrid molecular wire that was synthesized here is abbreviated as Ru-OPP.

Layer thickness for all self-assembled thin films was estimated by ellipsometry. Ellipsometric data were acquired for each gold substrate prior to and immediately after surface modification. Ellipsometric thickness for the OPP monolayer (19.4 ± 0.1 Å), Pt-OPP (24.4 ± 0.1 Å), and Ru-OPP (28.9 ± 0.1 Å) formed by the two-step methods is in close agreement with the calculated thickness of the molecules, suggesting a nearly upright configuration for these organic films. However,

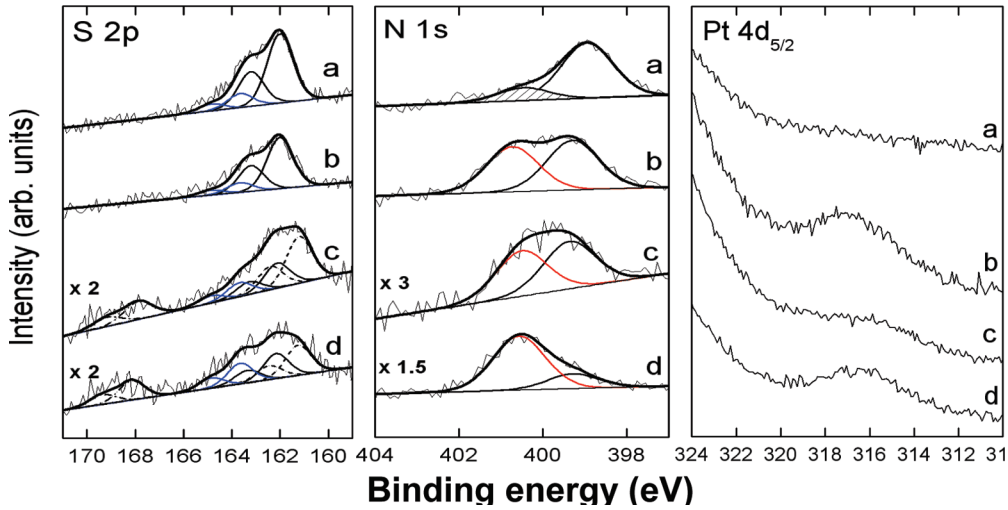

Figure 3. XPS core level spectra of (a) OPP/Au, (b) Pt-OPP/Au, (c) Pt-OPP(direct)/Au with base-promoted deprotection, and (d) Pt-OPP(direct)/Au without base deprotection in S 2p, N 1s, and Pt $4d_{5/2}$ regions.

ellipsometric thickness of Pt-OPP formed by the direct assembly was measured to be 14.4 Å; this is half the theoretical height of the upright molecule, suggesting the molecular wire displays a large molecular tilt (~60°) relative to the surface normal.

X-ray photoelectron spectroscopy confirms the self-assembly of the OPP monolayer. As shown in Figure 3, the formation of a gold−thiolate link is verified by the occurrence of the S $2p_{3/2}$ peak at ~162 eV.[15] The presence of a peak at ~168 eV assignable to oxidized thiolate[16] was observed only for the Pt-OPP film formed by direct assembly; it was absent in the OPP SAM or in the Pt-OPP formed by the two-step process. This indicates that the direct assembly of Pt-OPP did not give a well-packed monolayer compared to the two-step process. In addition, the binding energy of the Pt $4d_{5/2}$ peak displayed by the directly assembled Pt-OPP film is 0.8 eV lower than that exhibited by Pt-OPP formed *via* the two-step assembly. The lower binding energy displayed by the directly assembled film is consistent with the flat-lying orientation proposed earlier based on its ellipsometric thickness. The large molecular tilt from the surface normal and proximity of the Pt(II) moieties to the gold surface lowered its binding energy.[17] The N 1s spectra of the molecular films can be deconvoluted into two halves. The lower binding energy component at ~399 eV can be assigned to the free pyridine N atoms of the OPP.[18] The extent of coordination of the pyridinium N to other species can be judged from the intensity of a second peak at ~400.5 eV. In the case of OPP, the small peak at 400.5 eV is due to the protonated pyridinium N. The intensity of this peak is observed to be stronger in Pt-OPP or Ru-OPP due to the dative bond formation between the pyridinium N and Pt^{II} metal center. Judging from the equal intensities of the two halves representing free and coordinated pyridine N, we could estimate that not more than 50% of the OPP was coordinated with the Pt transition metal complexes. This is expected since the ligand substitution reaction is a reversible reaction and equilibrium is achieved after prolonged incubation. The presence or absence of the counterions is also indicative of the type of bonding with the gold substrate. For example, no F signal can be detected in the Pt-OPP monolayer formed by the two-step method, suggesting the absence of PF_6^- counterions. One explanation is that the anchoring of the Pt-OPP on gold forms a compact layer and reduces the electrostatic interaction of the counterions and the metal center. A persistent F 1s peak indicative of electrostatically bound PF_6^- is present in the spectrum of the directly assembled Pt-OPP, suggesting that the direct assembly route results in physisorption of the transition metal complex on the surface.

Similarly, Ru-OPP inorganic−organic hybrid films were prepared *via* the facile axial ligation of $[Ru(terpy)(bipy)]^{2+}$ complexes to OPP monolayer. The XPS S 2p and N 1s spectra of Ru-OPP (Supporting Information S1) are similar to that obtained for Pt-OPP. Successful coordination of the Ru(II) complex is demonstrated by appearance of a Ru $3d_{5/2}$ peak at ~281 eV.[19] The AFM and STM images of the assembled Ru-OPP and Pt-OPP films are consistent with the formation of self-assembled monolayer (Supporting Information S2).

The structural integrity of the thin organic films was evaluated by performing cyclic voltammetry (CV) in the presence of a ferricyanide redox probe. The ability to block electron transfer between gold surface and redox species in solution depends on the surface coverage and level of defects in the films.[20,21] The cyclic voltammograms of the various films are shown in Figure 4. On the bare gold substrate, heterogeneous electron transfer proceeds without any impediment, resulting in closely spaced redox peaks which are characteristic of a quasi-reversible one-electron redox reaction. As shown, the self-assembled OPP on gold effectively blocks faradaic reaction on the electrode surface, which

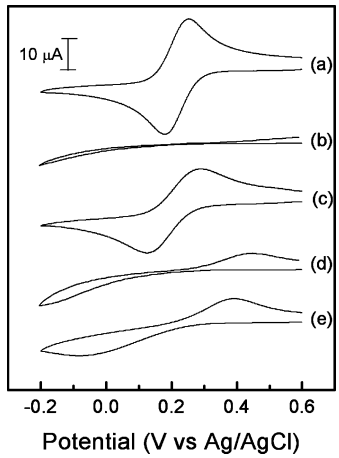

Figure 4. Cyclic voltammograms for (a) bare Au, (b) OPP/Au, (c) Pt-OPP(direct)/Au, (d) Pt-OPP/Au, and (e) Ru-OPP/Au in aqueous solution containing 1 mM $K_3Fe(CN)_6$ and 0.1 M KCl. Scan rate: 50 mV/s.

is indicative of the successful formation of a densely packed SAM. In contrast, the direct assembly of Pt-OPP on the Au substrate only slightly impedes the electron transfer; this implies the formation of a low-coverage film with high defect level. The faradaic currents increase slightly for the Pt-OPP and Ru-OPP hybrid molecular films, suggesting improved film conductivities upon coordination to transition metal complexes. This proves that, while the film conductivity is considerably enhanced, the strategy of coupling transition metal complexes onto the preassembled SAM does not cause any significant disruption to the integrity of the molecular layers.

The UV/vis absorption spectra of OPP, Pt(ĈN̂N)CH_3CN and Pt-OPP were recorded in dichloromethane solution at room temperature and are superimposed for comparison in Figure 5a. Due to its conjugated nature, OPP exhibits intense absorption bands (λ_{max} = 325 nm) attributable to $\pi\rightarrow\pi^*$ transitions.[22] Upon coordination to the platinum(II) complexes, a bathochromic shift is evident in the spectra of the resulting organometallic wire. Similar to the cyclometalated Pt(ĈN̂N)CH_3CN complexes, the resulting Pt-OPP hybrid molecules exhibit a weak and broad absorption band around the 400−500 nm region, which is due to metal-to-ligand charge transfer (MLCT) [(5d)Pt→π^*(CNN)],[23] whereas the intense absorption bands at $\lambda < 350$ nm could be attributed to intraligand transitions of the CNN ligand. Similarly, coordination of OPP to Ru(II) complexes resulted in a red shift in its UV/vis spectrum. The absorption spectra of the Ru-OPP and Ru(II) precursor complexes are dominated by spin-allowed $\pi\rightarrow\pi^*$ and $n\rightarrow\pi^*$ transitions of the ligands in the UV region of the spectra and by a MLCT band centered around 500 nm.[24,25] The bathochromic shifts for both systems, which are evident upon coupling of the transition metal complexes, suggest increased conjugation in the system. In addition, the MLCT band of the Ru(II) complex appears at a higher wavelength than that of the Pt(II) complex, suggesting that its HOMO−LUMO energy gap is smaller.

Square-planar Pt^{II} complexes display propensity to undergo Pt−Pt and/or ligand−ligand $\pi-\pi$ stacking in solutions and in the solid state. The emission spectra of PtII(pbipy-OPP)$^+$ complexes were observed to be concentration-dependent in dichloromethane. At low concentrations ($10^{-4}-10^{-6}$ mol dm^{-3}), an intense emission at 535 nm is observed. Increasing the concentration of the complex to 10^{-3} mol dm^{-3} results in suppression of the emission at 535 nm and the appearance of a new emission band centered at 680 nm (Supporting Information S2). Previous studies on mono- and dinuclear Pt^{II} derivatives have attributed the low-energy emission band to ligand−ligand ($\pi-\pi$) and metal−metal interactions.[26,27] Figure 6 shows that the emission spectra of Pt-OPP hybrid films prepared *via* either the two-step procedure or direct assembly method exhibit sharp emission at 678 nm arising from Pt−Pt and/or $\pi-\pi$ interactions between the aromatic

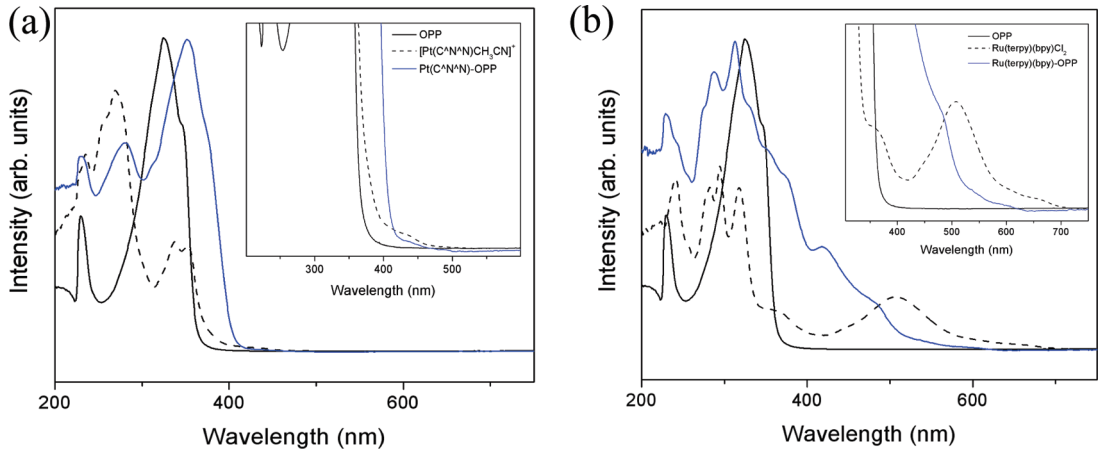

Figure 5. Absorption spectra of (a) OPP (solid and black line), Pt(ĈN̂N)(CH_3CN) · PF_6 (dashed line), and Pt(ĈN̂N)(OPP) · PF_6 (blue line) collected in dichloromethane at 298 K and superimposed for comparison; (b) OPP (solid and black line), Ru(terpy)(bpy)Cl_2 (dashed line), and Ru(terpy)(bpy)(OPP) · PF_6 (blue line) collected in dichloromethane at 298 K and superimposed for comparison.

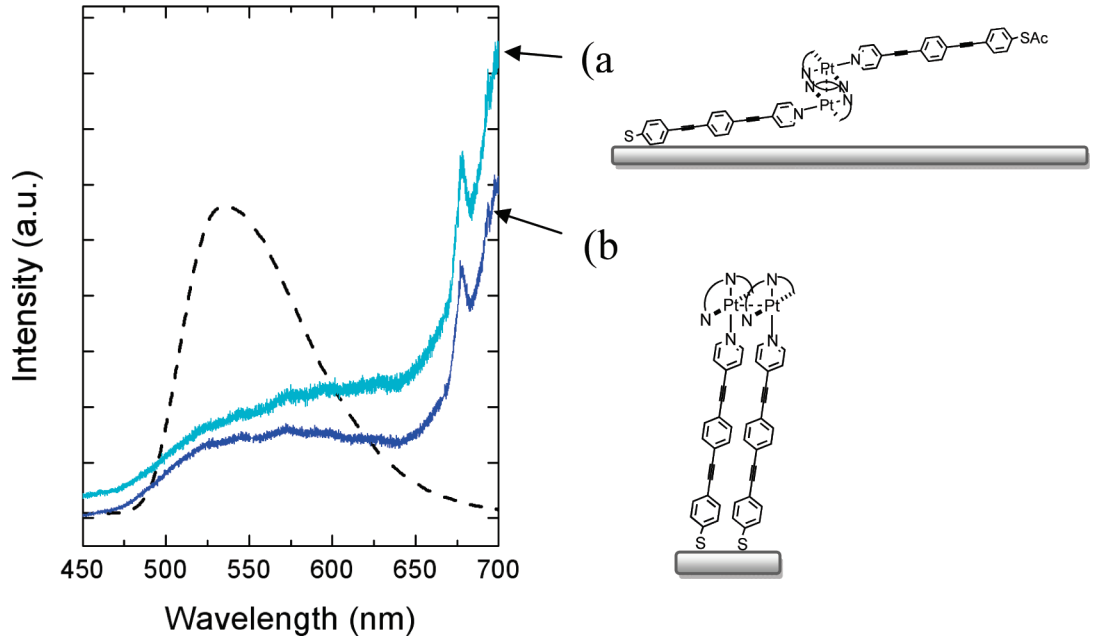

Figure 6. (a) PL spectra of directly assembled Pt-OPP on gold (cyan) and (b) Pt-OPP monolayer *via* two-step assembly (blue) superimposed with emission spectrum of Pt-OPP solution in dichloromethane (black, dashed). Strong bands at 678 nm arise due to stacking of Pt(II) complexes on Au surfaces. The illustrations on the right show the stacking due to metal−metal interactions.

ligand moieties. Monomeric luminescence is greatly diminished and red-shifted to $\lambda_{max} = 570$ nm. Both samples exhibit equally intense emission peaks, indicating that both direct assembly and two-step coupling methods were mediated by $\pi-\pi$ stacking of Pt(II) moieties. The proposed structures of the stacking arrangement in both samples are presented on the right panel of Figure 6. To the best of our knowledge, this work provides the first experimental evidence of stacked arrangement of Pt^{II} complexes in the Pt-OPP monolayer.

The electrical conductance of the SAMs was probed using three test beds. In the first method, SAMs were sandwiched between metal electrodes to form large-area molecular junctions, and the average film properties were studied. The other two methods applied are conducting-probe atomic force microscopy (AFM) and scanning tunneling microscopy (STM).

Sandwich Device Measurement. In Figure 7, the current density (*I*) is plotted on a logarithmic scale as a function of the applied voltage (*V*). The measured current of the bare junction without a SAM is several orders of magnitude larger compared to the junction with the SAM; this proves that the measured currents were modulated by the resistance of the molecular wire. Junctions containing the OPP monolayer show slight rectifying behavior with higher currents at negative substrate bias voltage. The measured current density of the transition metal complex−OPP monolayer is much larger than that of the OPP within the applied voltage window. In addition, it shows opposite rectification to that of OPP with higher currents observed at positive applied bias. The rectification ratios (RR = $I(+1.0\ V)/I(-1.0\ V)$) are 2.25 and 2.4 for junctions containing Pt(II) and Ru(II)complexes, respectively.

Scanning tunneling microscopy (STM) and atomic force microscopy (AFM) *I*−*V* provide a localized probe of the charge transport characteristics. As shown in Figure 8, these local transport measurements confirmed that measured current in the transition metal complex−OPP molecular layer is higher than that of the OPP layer, similar to results obtained in device measurements. The Pt-OPP and Ru-OPP molecular layers exhibit currents 1 order of magnitude higher than that of OPP. In addition, the hybrid films show negative differential resistance (NDR) features in both positive and negative regions. NDR typically appears at ~0.8 V in the case of Pt^{II} complexes, while for Ru^{II} complexes, NDR peaks start appearing at a bias around 0.6 V. Using AFM-IV, 75% of the transition complex−OPP molecular films probed displayed NDR peaks. The proportion of films exhibiting NDR phenomena was determined to be 85% by STM *I*−*V* measurements. Histograms showing the frequency of NDR peaks at various applied bias voltages are shown in Supporting Information (Figure S6). Both AFM *I*−*V* and STM *I*−*V* results show that Ru-OPP exhibits NDR peaks at lower bias voltages than Pt-OPP.

Transition metal−OPP molecular films consistently showed higher conductance values compared to OPP SAM on all three conductivity measurement platforms. In the OPP monolayer, the dominant conduction mechanism is believed to be nonresonant (direct) tunneling within the bias window. Upon coordination of the transition metal complexes to the terminal pyridyl moieties of OPP monolayer, d orbitals are introduced into the gaps of the π-electronic system, giving rise to a

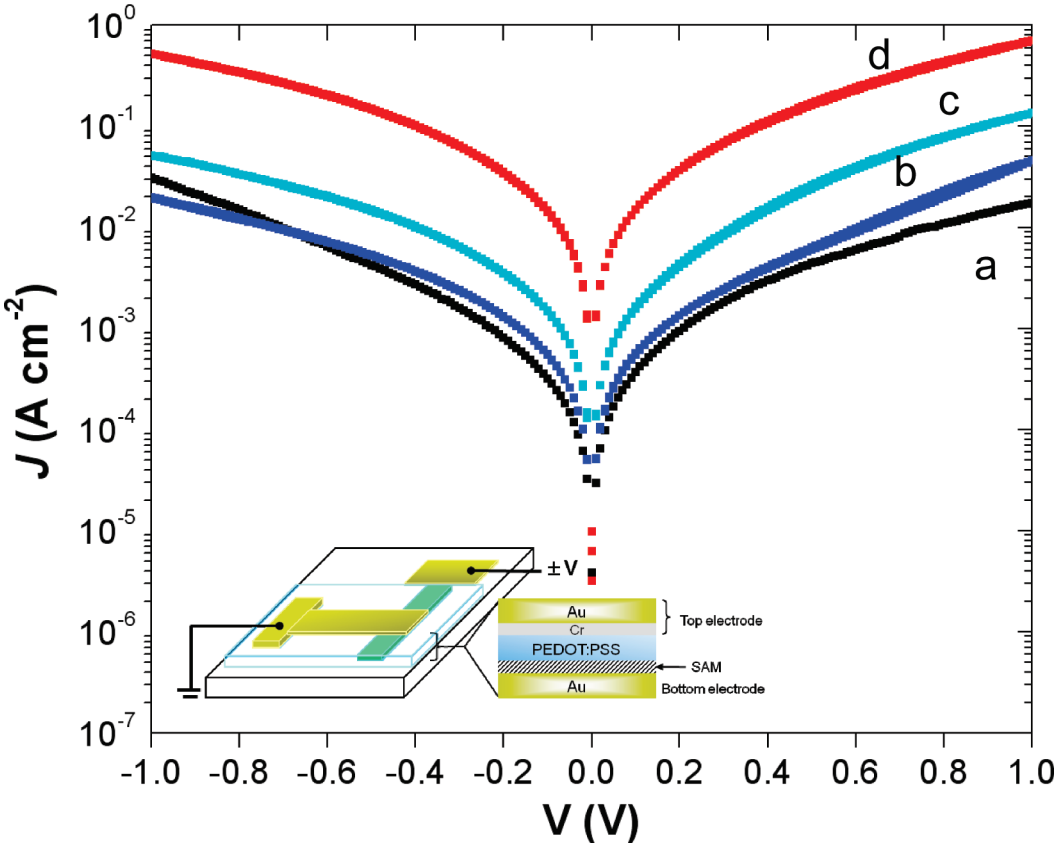

Figure 7. Current density plotted as a function of voltage bias on logarithmic scale for (a) OPP/Au, (b) Pt-OPP/Au, (c) Ru-OPP/Au, and (d) Pt-OPP(direct)/Au. Inset shows the sandwich device configuration in a single molecular junction. Voltage bias was applied to the bottom contact, while the top contact was grounded.

smaller HOMO−LUMO gap. The d orbitals of the transition metal complexes provide additional resonance channels for charge transport compared to the π orbitals in the OPP molecular wire. Due to the dipolar field along the molecular axis, a small positive bias will bring the Fermi level of the ungrounded electrode into resonance with the filled frontier orbitals.

In principle, since the hybrid molecular wire consists of a metal center, which acts as an electron acceptor linked to an organic chain acting as an electron donor, it has the intrinsic property of a rectifying junction. Dipole moments present in Pt-OPP and Ru-OPP molecular wires are calculated to be 15.12 and 27.54 Debye, respectively. The molecular dipole moment for OPP is directed toward the thiolate end anchored on the substrate. In the case of transition metal−OPP molecular films, the molecular dipole moments are directed in the opposite direction instead, that is, toward the STM tip. In the Pt-OPP or Ru-OPP molecular wire, the LUMO is concentrated mainly at the central metal ion, while HOMO is located on the OPP bridging ligand toward the thiol end. The preferred electron flow would therefore be electron injection from the STM tip into the LUMO of the metal complex and electron transfer from the HOMO to the positively biased substrate. We observed that over 65% of the measured hybrid films indeed showed higher tunneling current at positive sample bias, while the rest exhibited the opposite rec-

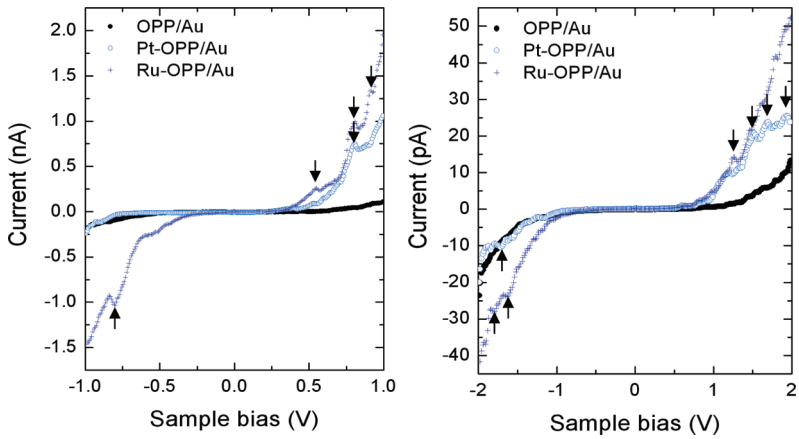

Figure 8. *I*−*V* curves measured by contact atomic force microscopy (c-AFM) (left) and scanning tunneling spectroscopy (STS) (right) for OPP/Au, Pt-OPP/Au, and Ru-OPP/Au. Polarity shown corresponds to sample bias. STM tip position was initially set to provide tunneling current of 2 pA at 1.0 V. Black arrows indicate occurrence of weak NDR features.

tifying behavior. However, the current rectification ratio (~2.2−2.4) observed in the hybrid molecular wire is smaller than expected. The lack of strong rectification in this molecular wire may be due to two reasons. One is the nature of the asymmetrical metal−molecule coupling at the two terminals. For the Pt-OPP or Ru-OPP, one end of the molecular wire is attached by a thiolate bond to gold, while the other end is terminated by the transition metal complex that is not covalently bonded to the other electrode. In the presence of asymmetrical interface, localized charge on the molecule can get closer to one electrode compared to the other, and this will build a greater image-type stabilization and yield an asymmetry in the overall electrostatic potential. The asymmetrical interface also imposes an opposing effect on the lineup of the electrode Fermi levels relative to the effect of dipole moment, thus reducing the overall rectification effect. The second reason is that the coverage of the transition metal complex is not 100% on the OPP monolayer. Over 65% of the measured hybrid films showed higher tunneling current at positive sample bias than at negative bias, while the rest exhibited the opposite rectifying behavior. The opposite rectifying behavior might be due to the STM tip contacting parts of the OPP film which are not coordinated to any metal complexes. The discrepancies between the relative rectification ratios displayed by Pt-OPP and Ru-OPP using AFM/STM compared to large-area device measurements are due to differences in contact resistance of the area probed. If the STM probe interrogates a stacked arrangement of Pt-OPP, a more pronounced rectification may be recorded compared to the measurement on Ru-OPP films since the molecules in the latter film do not cluster together as much as Pt-OPP. However, on a large lateral scale, the Ru-OPP thin film shows greater rectification than the Pt-OPP thin film due to its higher molecular dipole moment.

The hybrid molecular films also exhibit NDR signatures, such as an initial rise in current followed by a sharp decrease when the voltage is progressively augmented. It is noteworthy that no NDR is observed for the OPP molecular wire within the bias window, but distinct NDR peaks could be observed for the transition metal−OPP molecular wire.

Theoretical computation based on first-principles density functional theory (DFT) combined with nonequilibrium Green's function technique (NEGF) was performed to investigate how the NDR effects arise in the Ru-OPP or Pt-OPP molecular wire. The simulated current−voltage curve shows NDR effects for the Ru-OPP and Pt-OPP within the bias window, but this effect is absent in OPP (Supporting Information S4). Insights into the influence of transition metal complex on the electronic structure of the hybrid molecular wire can be obtained by examining the equilibrium transmission spectra, the frontier orbitals of the molecular projected self-consistent Hamiltonian (MPSH), as well as the density of states projected on the molecule (PDOS). Figure 9 plots the transmission spectrum (black) and partial density of states (PDOS) (blue) as a function of electronic energy at zero bias for OPP, Pt-OPP, and Ru-OPP. The isosurface diagrams of selected MPSH orbitals, associated with the PDOS peaks, are also shown. The LUMO of OPP shows significant delocalization throughout the entire molecular wire. The OPP is covalently coupled to the lead at one end *via* the Au−S thiol bond and at the other lead by the coordination between the pyridinyl terminal and the metal contact. The effective coupling to the leads at both ends gives rise to broad transmission peaks.[28] In the case of Pt-OPP or Ru-OPP, the frontier orbitals are localized mainly at transition metal moieties. The ligands surrounding the transition metal complex precluded strong coupling to the lead at that end. The absence of strong coupling with the lead and lack of delocalized orbital network in Pt-OPP or Ru-OPP structures results in sharp transmission peaks. Enhanced conductance in these hybrid wires at low bias arises from resonant conduction through localized states lying near the Fermi level. The appearance of the NDR peaks observed in the STM $I-V$ measurement in Figure 8 is related to changes in transmission function and the occurrence of energy resonance among the electronic levels for a limited range of applied electrical field.

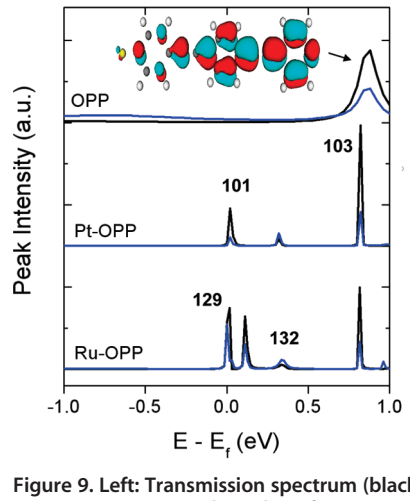

n	ε_n (eV)	MPSH orbital
101 Pt-OPP	0.024	
103 Pt-OPP	0.822	
129 Ru-OPP	-0.0012	
132 Ru-OPP	0.328	

Figure 9. Left: Transmission spectrum (black) and PDOS (blue) as a function of electronic energy at zero bias show for OPP, Pt-OPP, and Ru-OPP. Right: Isosurface diagrams of selected MPSH orbitals contributing to transmission within ±0.5 eV from Fermi energy (taken to be 0 eV).

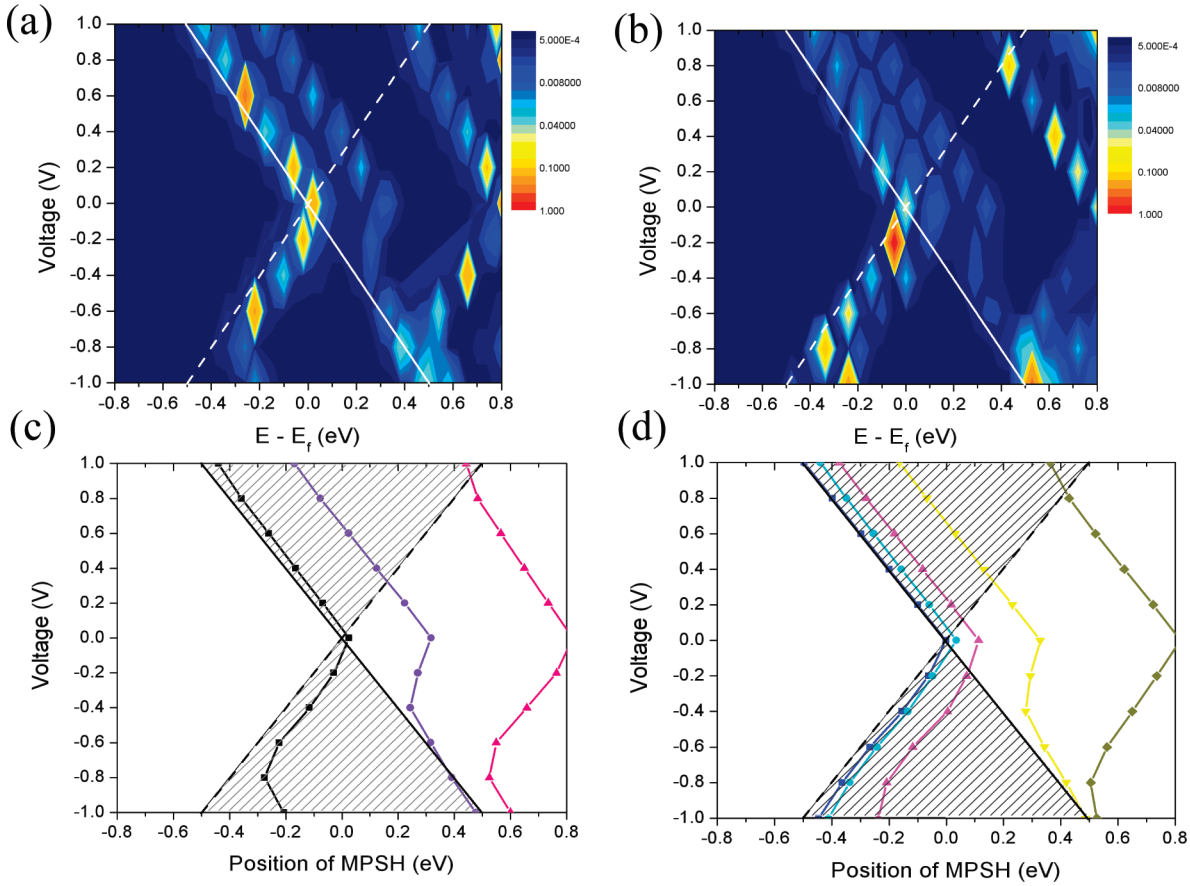

Figure 10. Evolution of transmission probability (represented in the *z*-axis by color intensity) as functions of electronic energy and bias voltage for (a) Pt-OPP and (b) Ru-OPP. A higher color intensity indicates a higher transmission probability. The shift in positions of the MPSH orbitals (refer to Figure 9) with respect to applied voltage bias for (c) Pt-OPP and (d) Ru-OPP. The triangle defined by the lines is the bias window. Solid and dashed lines refer to the electrochemical potentials of the left and right leads, respectively.

To understand the mechanism of NDR behavior in organometallic wires, the evolution of transmission function with applied voltage is examined in Figure 10. The shift in the transmission peaks is observed to follow closely the eigenvalues of the MPSH orbitals. Only MPSH orbitals that fall within the bias window will contribute to conduction. The MPSH orbitals respond differently under applied voltage according to their relative strength of coupling to the left and right leads, as shown in Figure 10c,d. Molecular orbitals localized at OPP generally follow the chemical potential of the left lead to which the molecules are anchored *via* the Au−S bond. On the other hand, molecular orbitals localized at the transition metal are observed to follow the chemical potential of right lead at positive bias and that of left lead at negative bias due to potential drop over the vacuum gap. At a limited range of applied voltage, these molecular orbitals move toward each other and overlap, giving rise to greater delocalization and higher current, thus producing a current spike. Beyond a certain threshold voltage, the molecular orbitals move apart and the current density drops, which rationalizes the appearance of the NDR peak.

CONCLUSIONS

In summary, we have demonstrated that the coupling of transition metal complexes to preassembled OPP SAM is the choice method for the fabrication of organic−inorganic hybrid molecular ensemble. Hybrid molecular films prepared this way exhibit a higher packing density and orientational order compared to those formed *via* direct assembly of the synthesized molecules. The poorer quality of the hybrid molecular films formed by direct assembly is due to the labile metal−N bond, which is susceptible to attack by base. Several interesting electronic and structural effects result from the molecular wire with the coupled transition metal cluster. There is evidence of π−π stacking between hybrid molecular wires, and such lateral interaction may have a role toward protecting the molecular electronic functionality and stabilizing the assembled molecule on a given substrate. Electrical measurements show that, at low bias voltages within ±0.5 V, the hybrid molecular wire behaves like a molecular conductor, and the overall conductance of the hybrid molecular wire is higher compared to the organic-only molecular wire. This provides evidence of strong electronic coupling between the transi-

tion metal complex and the organic chain following the coupling of the transition metal complex onto the pyridinyl terminal of the OPP molecular wire. Nonlinear electron transport phenomena only appear at higher bias voltages, opening up possibilities for applications in various fields of molecular electronics. The presence of the transition metal complexes in the hybrid molecular wire with asymmetrical coupling at the two electrode terminals exhibits distinctive NDR effects. In the future, it is possible to extend the design to the (organic chain)−(metal cluster)−(organic chain) system such that symmetrical contacts to the leads can be formed at two ends. It can be envisaged that molecular scale patterning of the transition metal cluster on the preassembled organic SAM can allow nanojunctions with unique switching or memory effects to be developed.

EXPERIMENTAL SECTION

1-((4-Acetylthiophenyl)ethynyl)-4-((4-pyridyl)ethynyl)benzene (OPP). To deaerated dry THF (100 mL) were added 1-[4-(*S*-acetylthiomethyl)phenyl]acetylene (1.5305 g, 8.70 mmol), 4-iodophenylethynylpyridine (2.654 g, 8.70 mmol), 20 mL of diisopropyl ethylamine, $Pd_2(dba)_3$ (270 mg, 0.261 mmol), CuI (50 mg, 0.261 mmol), and PPh_3 (410 mg, 1.566 mmol). The mixture was stirred under N_2 for 2 days at 30 °C and then filtered and washed with chloroform. The solvent was removed by rotaevaporation, and the resulting mixture was separated with column chromatography (silica gel, hexane/dichloromethane v/v = 2:1). The product was obtained as an off-white solid (yield 35%): ^{1}H NMR (300 MHz, in $CDCl_3$) δ 8.66 (br s, 2H, $H_{2,6}$), 7.58−7.40 (m, 10H, aromatic protons), 2.45 (s, 3H, CH_3); EI-MS (*m*/*z*, ra) 311.1 $[M - CH_3CO]^+$ (100%), 353.1 $[M]^+$ (40%).

Pt(pbipy)(OPP) · PF_6: A mixture of Pt(pbipy)(CH_3CN) · PF_6 (100 mg, 0.16 mmol) and OPP (57 mg, 0.16 mmol) was stirred in $MeCN/CH_2Cl_2$ (v/v = 1:1, 10 mL) at room temperature for 24 h. Addition of excess diethyl ether to the solution precipitated the product as yellow solids. The compound was purified by recrystallization from CH_3CN/diethyl ether: ^{31}P,^{1}H NMR (300 MHz, in acetone-d_6) δ 9.22 (d, 2H, $^2J_{H-H}$ = 7 Hz, $^3J_{H-Pt}$ = 40 Hz, $H_{2,6}$ of pyridine ligand (PY)), 8.60−8.58 (m, 1H, $H_{6'}$ of 6-phenyl-2:2′-bipyridine (NNC)), 8.48−8.45 (m, 1H, $H_{5'}$ of NNC), 8.40−8.38 (m, 1H, $H_{3'}$ of NNC), 8.26−8.25 (m, 2H, $H_{3''}$ of PY), 8.08−8.05 (m, 1H, H_4 of NNC), 7.99 (d, 2H, J_{HH} = 7 Hz, $H_{3,5}$ of PY), 7.92−7.87 (m, 1H, $H_{6''}$ of NNC), 7.78−7.64 (m, 7H, $H_{2',2''}$ of PY, $H_{3,4,5}$ of NNC), 7.51 (d, 2H, J_{HH} = 9 Hz, $H_{3'}$ of PY), 7.18−7.16 (m, 2H, $H_{4'',5''}$ of NNC), 6.52−6.49 (m, 1H, $H_{3''}$ of NNC). Anal. Calcd for $C_{38}H_{26}PtN_3F_6POS$: C, 50.00; H, 2.85; N, 4.1. Found: C, 50.23; H, 2.92; N, 4.45.

Ru(terpy)(bipy)(OPP) · $2PF_6$: A mixture of Ru(terpy)(bipy)(CH_3CN) · PF_6 (130 mg, 0.16 mmol) and OPP (57 mg, 0.16 mmol) was stirred in $MeCN/CH_2Cl_2$ (v/v = 1:1, 10 mL) at room temperature for 24 h. Addition of excess diethyl ether to the solution precipitated the product as purple solids. The compound was purified by recrystallization from CH_3CN/diethyl ether: ^{1}H NMR (300 MHz, in CD_3CN) δ 8.71−8.65 (m, 2H, bpy), 8.52 (d, J_{HH} = 8 Hz, 2H, $H_{3,5}$ of tpy), 8.43 (d, J_{HH} = 8 Hz, py), 8.40 (d, J_{HH} = 8 Hz, 1H, bpy), 8.32−8.29 (m, 1H, bpy), 8.21 (t, J_{HH} = 8 Hz, 1H, H_4 of tpy), 8.04−8.00 (m, 2H, tpy), 7.86−7.82 (m, 2H, bpy), 7.77−7.40 (unresolved multiplets, 14 H), 7.26−7.24 (m, 3H), 7.08−7.04 (m, 1H, bpy), 2.40 (s, 3H, CH_3); ESI-MS (*m*/*z*, ra) 422.1 $[M - 2PF_6]^{2+}$ (100%), 988.9 $[M - PF_6]^+$ (10%). Anal. Calcd for $C_{47}H_{34}RuN_6F_{12}P_2OS$: C, 50.31; H, 3.03; N, 7.41. Found: C, 51.01; H, 3.31; N, 7.83.

Materials. Ammonium hydroxide (Aldrich, 30% NH_4OH in water) and anhydrous acetonitrile (Aldrich, 99.8%) were used as received. Tetrahydrofuran was purified by distillation over metallic sodium and benzophenone under a nitrogen atmosphere. Milli-Q grade water (>18 MΩ) was used for preparation of electrolyte solutions in electrochemical experiments. Glasswares were routinely cleaned using aqua regia (3:1 concentrated HCl/concentrated HNO_3).

Electronic Structures of Isolated Molecules. UV/vis spectra of OPP, Pt(pbipy)(OPP) · PF_6, and Ru(terpy)(bipy)(OPP) · $2PF_6$ in dichloromethane were recorded on a Shimadzu UV-2450 spectrophotometer under ambient conditions. Emission spectra of Pt(pbipy)(OPP) · PF_6 were obtained on Perkin-Elmer LS 55 fluorescence spectrometer.

Electronic structures and dipole moments of the isolated molecules were calculated using B3PW91 hybrid DFT with LanL2DZ basis set for all the atoms as implemented in the GAUSSIAN 03 program.

Monolayer Preparation. Self-assembled monolayers (SAMs) were prepared on two types of gold surfaces, namely, gold-coated silicon (100) wafers (Platypus Technologies) and gold/mica substrates (SPI, West Chester, PA). These substrates are polycrystalline with a predominant (111) orientation.[29,30] Au/Si wafers were cleaned immediately prior to use by soaking in piranha solution (3:1 concentrated H_2SO_4/30% H_2O_2) at 60 °C for 10 min, followed by thorough rinsing with ultrapure water. Au/mica substrates were cleaned by a few sputter-anneal cycles in UHV chamber before self-assembly. OPP monolayers were prepared by immersing Au substrates into 0.5 mM solution of OPP in freshly distilled THF for 20−24 h. Ten microliters of 30% NH_4OH was added for *in situ* deprotection 5−10 min before introducing Au substrates.

Direct assembly of Pt(pbipy)(OPP) · PF_6 was carried out by immersing the gold substrate in a dichloromethane solution of Pt(pbipy)(OPP) · PF_6 without deprotection as addition of NH_4OH was found to result in side reactions. The transition metal complexes were alternatively attached to the terminal pyridyl moieties of the preassembled OPP SAM by axial ligation. In this case, Au substrates prefunctionalized with OPP SAM were incubated in ~1 mM solution of Pt(pbipy)(CH_3CN) · PF_6 in anhydrous acetonitrile for 2 days to form Pt-OPP SAM. Ru-OPP SAM was prepared similarly by heating OPP-modified gold substrates in 1 mM of Ru(terpy)(bipy)Cl · $2PF_6$ solution under nitrogen atmosphere.

Surface Characterization. X-ray photoelectron spectroscopy (XPS) was performed with a VG ESCA Mark II spectrometer equipped with an unmonochromatized Mg Kα X-ray source ($h\nu$ = 1253.6 eV) and hemispherical electron analyzer. Survey spectra were acquired with a pass energy of 50 eV, while high-resolution spectra were acquired with a pass energy of 20 eV. The analyzer pass energy was maintained at 50 eV for single sweep survey scans and 20 eV for high-resolution narrow scans. Spectral analysis included a linear background correction followed by peak deconvolution with mixed Gaussian−Lorentzian functions. The binding energies were referenced to Au $4f_{7/2}$ peak at 84.00 eV.

Layer thickness for all of the self-assembled thin films was estimated by ellipsometry (J.A. Woollam M-2000 variable angle spectroscopic ellipsometer). Ellipsometric data were collected at angles of 60, 65, and 70° over a wavelength range of 400−1000 nm for each gold substrate prior to and immediately after surface modification. Data analysis was performed using WVASE32 software package. Optical constants of clean gold substrate were first determined by fixing its thickness at 1000 Å (as provided by commercial manufacturer). The optical constants of the gold surface were used in subsequent fitting of the thickness of the self-assembled films. The fitting procedure was based on Cauchy model, using a refractive index of 1.80 for all. The average thickness determined from three similar samples was reported. Samples were stored under nitrogen atmosphere to avoid oxidation of the molecules.

Cyclic voltammetry (CV) was performed in a conventional three-electrode electrochemical cell with geometric area of the working electrode defined by the size of an inert elastomer O-ring (0.0707 cm^2). Ag/AgCl (3 M KCl) and large-area platinum mesh were used as reference and counter electrodes, respectively. Electrolyte solutions were prepared with ultrapure water (resistivity = 18.2 MΩ · cm) and nitrogen-purged for at least 20 min before experiments. Cyclic voltammograms were collected

with Autolab PGSTAT30 digital potentiostat/galvanostat coupled with GPES 4.9 software (Eco Chemie, The Netherlands) and a Lock-In Amplifier (PAR EG&G model 273A). Electrochemical blocking experiments were conducted in an aqueous solution of 1 mM $K_3[Fe(CN)_6]$ with 0.1 M KCl as supporting electrolyte between −0.2 and +0.6 V at a scan rate of 50 mV/s.

Photoluminescence (PL) measurements of Pt-OPP films on gold were performed by excitation at $\lambda = 325$ nm with a pulsed laser using micro-Raman/PL spectrometer (Renishaw, 325 nm, 40 mW).

Current−Voltage (*I*−*V*) Characterization. Patterned Cr (50 Å) and Au (500 Å) bottom contacts were evaporated through shadow mask onto glass substrates (15 × 15 mm^2). The substrates were cleaned using oxygen plasma before immersion into solution of precursor molecules for self-assembly to proceed. After film deposition, the substrates were rinsed thoroughly and dried with gentle flow of N_2. PEDOT/PSSH/surfactant (1:16:0.01) was then spin-coated over the self-assembled films to prevent electrical shorts during evaporation of the top metal contact. Finally, Cr/Au top contacts were evaporated through a shadow mask to form 0.1 × 0.1 mm^2 molecular junctions. *I*−*V* measurements were performed using a Keithley 4200 semiconductor parameter analyzer using a probe station in a N_2-purged glovebox. Such sandwich devices were fabricated for *I*−*V* characterization for all samples. Control devices without a SAM were also prepared and measured to ensure the *I*−*V* curve for PEDOT/PSS layer alone is ohmic and does not dominate the *I*−*V* curves recorded for the samples. Parasitic currents through the overlaying conducting polymer were verified to be negligible by measuring current response between two adjacent (top or bottom) contacts.

Conducting-probe atomic force microscopic (CP-AFM) measurements were performed using a XE-100 AFM (PSIA Corp.) instrument. The AFM tips used were commercially available silicon cantilevers coated with conductive Au−Cr film (nominal force constant 3.5 N/m). Junctions were formed by contacting conductive tips under a controlled load of 2 nN with the sample surface. The tips were not scanned over the surface to prevent scratching the gold coating. In our setup, the sample was isolated from ground and a voltage was applied on the sample under software control. The tip current was read by a current-to-voltage converter (Femto LCA 200-100G). Multiple samples of each monolayer were studied. Constant normal load of ~2 nN was applied during all of the measurements, and each sample was tested with 3−4 new tips. Ten to 15 *I*−*V* curves were recorded with each tip at different locations by sweeping voltage between ±1.0 V under constant applied load.

STM measurements were performed at room temperature under ambient conditions. Mechanically cut Pt−Ir (80:20) tips were used for imaging and current−voltage acquisitions with bias applied to sample. Topographic images were obtained in constant current mode with large tunnel junction impedances of 50 GΩ/1 TΩ to avoid destructive tip−surface interactions. During the sweep of bias voltage, the tip−sample distance was held fixed by interrupting feedback to *z*-piezo and the current was recorded. To minimize tip artifacts, the electronic data were averaged from 30 *I*−*V* curves per sample that were taken at random points using several freshly clipped tips per sample.

Theoretical *I*−*V* Calculation. To construct the molecular wire junctions, the geometries of the molecules and semi-infinite electrodes were first optimized with molecular dynamics. Au(111)-(3 × 3) surfaces were used to construct OPP molecular junction, while larger (5 × 5) Au leads were used in OPP junctions incorporating transition metal complexes to avoid any interaction between the bulkier molecules in the next supercell. The optimized molecules were positioned between the electrodes with the thiol end forming a chemical bond at the hollow site of the left gold electrode, while an arbitrary gap of 2.5 Å was inserted between the right electrode and molecules to simulate the absence of a chemical bond.

The electron transport properties of the molecular wires were investigated using first-principles computational package, Atomistix ToolKit (ATK), which is based on nonequilibrium Green's function (NEGF) combined with density functional theory (DFT).[31] This method can treat the molecule−electrode system self-consistently under finite bias condition. The effects of bulk electrodes are considered through self-energy, which are effective Hamiltonians arising from the coupling of molecule with electrodes. Norm-conserving pseudopotentials are adopted to describe the electron-ion interactions. NEGF is used to calculate the charge distribution for the systems. We used double-ζ plus polarization (DZP) basis set for all atoms except Au, for which single-ζ plus polarization (SZP) basis was used. Perdew−Zunger local density approximation (LDA) functional is adopted for exchange-correlation.

The transmission function $T(E,V)$ of the system is a sum of transmission probabilities of all channels available at energy E under external bias. The electric current as a function of the applied voltage is then obtained by integration of transmission spectrum (Landauer formula):[32]

$$I(V) = \frac{2e}{h}\int_{\mu_{min}}^{\mu_{max}} dE(f_L(E,V) - f_R(E,V)\cdot T(E,V)$$

where $f_L(E,V)$ and $f_R(E,V)$ are the Fermi−Dirac functions for the left and right electrodes at energy E under bias voltage V. The bias window is given by $\mu_R = E_f + eV_{bias}/2$ and $\mu_L = E_f - eV_{bias}/2$, where E_f is the Fermi energy.

Acknowledgment. K.P.L. thanks ARC-MOE Grant R-143-000-344-112 "Structure and Dynamics of Molecular Self-Assembled Layers." N.Z. thanks Chia Perq Jon for his help.

Supporting Information Available: Detailed XPS data; emission spectra of $[Pt^{II}(pbipy)(OPP)]\cdot PF_6$ in dichloromethane; AFM topography images of self-assembled layers; histograms showing frequency of NDR occurrences *etc*. This material is available free of charge *via* the Internet at http://pubs.acs.org.

REFERENCES AND NOTES

1. Paul, F.; Lapinke, C. Organometallic Molecular Wires and Other Nanoscale-Sized Devices. *Coord. Chem. Rev.* **1998**, *178*−*180*, 451–509.
2. Joachim, C.; Ratner, M. A. Molecular Electronics: Some Views on Transport Junctions and Beyond. *Proc. Natl. Acad. Sci. U.S.A.* **2005**, *102*, 8801–8802.
3. Lee, Y.; Yuan, S.; Sanchez, A.; Yu, L. Charge Transport Mediated by d-Orbitals in Transition Metal Complexes. *Chem. Commun.* **2008**, 247–249.
4. Li, Z.; Kosov, D. S. Orbital Interaction Mechanisms of Conductance Enhancement and Rectification by Dithiocarboxylate Anchoring Group. *J. Phys. Chem. B* **2006**, *110*, 19116–19120.
5. Yan, L.; Bautista, E. J.; Seminario, J. M. *Ab Initio* Analysis of Electron Currents through Benzene, Naphthalene and Anthracene Nanojunctions. *Nanotechnology* **2007**, *18*, 485701.
6. Liu, R.; Ke, S.-H.; Baranger, H.; Yang, W. Organometallic Spintronics. *Nano Lett.* **2005**, *5*, 1959–1962.
7. Cedy, S. A.; Engtrakel, C.; Wang, L.; Liu, R.; Sita, L. R. Near Perfect Conduction through a Ferrocene-Based Molecular Wire. *Phys. Rev. B* **2005**, *71*, 241401-4.
8. Schull, T. L.; Kushmerick, J. G.; Patterson, C. H.; George, C.; Moore, M. H.; Pollack, S. K.; Shashidhar, R. Ligand Effects on Charge Transport in Platinum(II) Acetylides. *J. Am. Chem. Soc.* **2003**, *125*, 3202–3203.
9. Yokoyama, K.; Wakabayashi, A.; Noguchi, K.; Nakamura, N.; Ohno, H. Structure and Spectroelectrochemical Property of a Ruthenium Complex Containing Phenanthroline-Quinone, and Assembly of the Complexes on a Gold Electrode. *Inorg. Chim. Acta* **2006**, *359*, 807–814.
10. Chan, C.-W.; Lai, T.-F.; Che, C.-M.; Peng, S.-M. Covalently Linked Donor-Acceptor Cyclometalated Platinum(II) Complexes. Structure and Luminescent Properties. *J. Am. Chem. Soc.* **1993**, *115*, 11245–11253.
11. Brooks, J.; Babayan, Y.; Lamansky, S.; Djurovich, P. I.; Tsyba, I.; Bau, R.; Thompson, M. E. Synthesis and Characterization of Phosphorescent Cyclometalated Platinum Complexes. *Inorg. Chem.* **2002**, *41*, 3055–3066.

12. Tang, W.-S.; Lu, X.-X.; Wong, K. M.-C.; Yam, V. W.-W. Synthesis, Photophysics and Binding Studies of Pt(II) Alkynyl Terpyridine Complexes with Crown Ether Pendant. Potential Luminescent Sensors for Metal Ions. *J. Mater. Chem.* **2005**, *15*, 2714–2720.
13. Börje, A.; Köthe, O.; Juris, A. New Luminescent and Redox-Active Mono- and Polynuclear Ruthenium(II) and Osmium(II) Polypyridine Complexes. *J. Chem. Soc., Dalton Trans.* **2002**, 843–848.
14. Uehara, H.; Abe, M.; Hisaeda, Y.; Uosaki, K.; Sasaki, Y. Immobilization of a Binuclear Ruthenium(II) Complex on a Gold (111) Surface: Observations of Proton-coupled Electron Transfer and Electrochemical Durability in Aqueous Media. *Chem. Lett.* **2006**, *35*, 1178−1179.
15. Ishida, T.; Hara, M.; Kojima, I.; Tsuneda, S.; Nishida, N.; Sasabe, H.; Knoll, W. High Resolution X-ray Photoelectron Spectroscopy Measurements of Octadecanethiol Self-Assembled Monolayers on Au(111). *Langmuir* **1998**, *14*, 2092–2096.
16. Mekhalif, Z.; Riga, J.; Pireaux, J.-J.; Delhalle, J. Self-Assembled Monolayers of *n*-Dodecanethiol on Electrochemically Modified Polycrystalline Nickel Surfaces. *Langmuir* **1997**, *13*, 2285–2290.
17. Yang, Y. W.; Fan, L. J. High-Resolution XPS Study of Decanethiol on Au(111): Single Sulfur−Gold Bonding Interaction. *Langmuir* **2002**, *18*, 1157–1164.
18. Zubavichus, Y.; Zharnikov, M.; Yang, Y.; Fuchs, O.; Umbach, E.; Heske, C.; Ulman, A.; Grunze, M. X-ray Photoelectron Spectroscopy and Near-Edge X-ray Absorption Fine Structure Study of Water Adsorption on Pyridine-Terminated Thiolate Self-Assembled Monolayers. *Langmuir* **2004**, *20*, 11022–11029.
19. Mayer, C. R.; Dumas, E.; Miomandre, F.; Méallet-Renault, R.; Warmont, F.; Vigneron, J.; Pansu, R.; Etcheberry, A.; Sécheresse, F. Polypyridyl Ruthenium Complexes as Coating Agent for the Formation of Gold and Silver Nanocomposites in Different Media. Preliminary Luminescence and Electrochemical Studies. *New J. Chem.* **2006**, *30*, 1628–1637.
20. Cheng, L.; Yang, J.; Yao, Y.; Price, D. W., Jr.; Dirk, S. M.; Tour, J. M. Comparative Study of Electrochemically Directed Assembly *versus* Conventional Self-Assembly of Thioacetyl-Terminated Oligo(phenyleneethynylene)s on Gold and Platinum Surfaces. *Langmuir* **2004**, *20*, 1335–1341.
21. Maya, F.; Chanteau, S. H.; Cheng, L.; Stewart, M. P.; Tour, J. M. Synthesis of Fluorinated Oligomers towards Physical Vapor Deposition Molecular Electronics Candidates. *Chem. Mater.* **2005**, *17*, 1331–1345.
22. Hacker, C. A.; Batteas, J. D.; Garno, J. C.; Marquez, M.; Richter, C. A.; Richter, L. J.; van Zee, R. D.; Zangmeister, C. D. Structural and Chemical Characterization of Monofluoro-Substituted Oligo(phenylene-ethynylene) Thiolate Self-Assembled Monolayers on Gold. *Langmuir* **2004**, *20*, 6195–6205.
23. Wong, K.-H.; Chan, M. C.-W.; Che, C.-M. Modular Cyclometalated Platinum(II) Complexes as Luminescent Molecular Sensors for pH and Hydrophobic Binding Regions. *Chem.—Eur. J.* **1999**, *5*, 2845–2849.
24. Harriman, A.; Mayeux, A.; Nicola, A. D.; Ziessel, R. Synthesis and Photophysical Properties of Ruthenium(Ii) Bis(2,2′:6′,2″-terpyridine) Complexes Constructed from a Diethynylated-Thiophene Residue. *Phys. Chem. Chem. Phys.* **2002**, *4*, 2229−2235.
25. Medlycott, E. A.; Hanan, G. S.; Loiseau, F.; Campagna, S. Tuning the Excited-State Energy of the Organic Chromophore in Bichromophoric Systems Based on the Ru^{II} Complexes of Tridentate Ligands. *Chem.—Eur. J.* **2007**, *13*, 2837−2846.
26. Saito, K.; Hamada, Y.; Takahashi, H.; Koshiyama, T.; Kato, M. Organic Light-Emitting Diodes Based on a Binuclear Platinum(II) Complex. *Jpn. J. Appl. Phys.* **2005**, *44*, L500–L501.
27. Cocchi, M.; Virgili, D.; Fattori, V.; Rochester, D. L.; Williams, J. A. G. N^C^N-Coordinated Platinum(II) Complexes as Phosphorescent Emitters in High-Performance Organic Light-Emitting Devices. *Adv. Funct. Mater.* **2007**, *17*, 285–289.
28. Grigoriev, A.; Sköldberg, J.; Wendin, G. Critical Roles of Metal−Molecule Contacts in Electron Transport Through Molecular-Wire Junctions. *Phys. Rev. B* **2006**, *74*, 045401-1–045401-16.
29. Aguilar, M.; Anguiano, E.; Aznárez, J. A.; Sacedón, J. L. Rough Growth Fronts of Evaporated Gold Films, Compared with Self-Affine and Mound Growth Models. *Surf. Sci.* **2001**, *482−485*, 935–939.
30. Golan, Y.; Marqulis, L.; Rubinstein, I. Vacuum-Deposited Gold Films: I. Factors Affecting the Film Morphology. *Surf. Sci.* **1992**, *264*, 312–326.
31. Brandbyge, M.; Mozos, J.-L.; Ordejón, P.; Taylor, J.; Stokbro, K. Density-Functional Method for Nonequilibrium Electron Transport. *Phys. Rev. B* **2002**, *65*, 165401-1–165401-17.
32. Meir, Y.; Wingreen, N. S. Landauer Formula for the Current Through an Interacting Electron Region. *Phys. Rev. Lett.* **1992**, *68*, 2512–2515.